MNE 31 (2026) 100359

Contents lists available at ScienceDirect

Micro and Nano Engineering

journal homepage: www.elsevier.com/locate/mne

Research paper

The influence of proximity effects in electron beam lithography on integrated photonic systems ☆

Matthias L. Vermeer [a,*], Nadeem K. Alhareeb [a], Bojan Bosnjak [b], Robert H. Blick [b], Timo Lipka [a,*], Hoc Khiem Trieu [a]

[a] Institute of Microsystems Technology (MST), Hamburg University of Technology (TUHH), Am Schwarzenberg-Campus 1, Hamburg 21073, Hamburg, Germany
[b] Center for Hybrid Nanostructures (CHYN), Deutsches Elektronen-Synchrotron (DESY), Luruper Chaussee 149, Hamburg 22761, Hamburg, Germany

ARTICLE INFO

Keywords:
Microring resonators
Grating couplers
Electron beam lithography
Fabrication process variations
Deposited silicon
Integrated photonics
Silicon photonics

ABSTRACT

Testing and improving integrated photonic components and systems requires rapid prototyping of various design variations. Electron beam lithography enables such rapid prototyping, allowing adjustments on a run-to-run basis with minimum linewidths on the order of 10 nm. Process variations arising from focusing, stitching, and proximity effects can impact the fidelity of fabricated designs. These variations can be minimized by applying design-based or dose-based proximity correction schemes. In this work, both correction methods are applied to integrated photonic systems containing a microring resonator and uniform and apodized grating couplers fabricated on deposited silicon test samples. Their transmission spectra are experimentally measured and compared to theoretical predictions to evaluate the effectiveness of the proximity correction schemes.

1. Introduction

The combination of a high index contrast and the compatibility of silicon-on-insulator (SOI) photonics with integrated electronics has led to the rapid growth of silicon photonics. An unprecedented reduction in footprint and an increase in complexity and quality have been realized in passive and active SOI photonic circuits such as wavelength division multiplexers (WDMs) for telecommunication applications [1,2], optical neural network implementations for machine learning [3,4], and large-scale re-routing networks for universal quantum computing [5,6]. The use of numerous waveguides, microring resonators (MRRs), and Mach–Zehnder interferometers (MZIs) is crucial for the functionality of such circuits.

For testing and improving designs of photonic components, a large number of variations in design parameters must be considered. Rapid prototyping of test samples on SOI and other crystalline and deposited material platforms effectively reduces the design space in a short time and enables benchmarking of theoretical models against fabricated samples. Electron beam lithography (EBL) is an ideal method for rapid prototyping of photonic systems as it can generate device patterns with linewidths on the order of 10 nm without the need for photomasks, allowing design adjustments on a run-to-run basis [7,8]. Additionally, EBL is widely used for creating masters for nanoimprint lithography and for direct exposure in high-end applications requiring photonic nanostructures [9]. For passive photonic systems, EBL can be combined with direct laser writing of microheater structures to efficiently fabricate active photonic devices.

For fabricated photonic devices that correspond to the intended designs, the process deviations must be taken into account during the design phase. For example, the channel spacing of a wavelength division multiplexer can be stabilized by considering variations in waveguide height, widths of the two coupled waveguides, coupling gap and ring radius in designing the microresonator devices [10]. While height variations primarily result from polishing or deposition steps, width and shape variations mainly originate from lithography and etching processes [11]. For EBL, process variations and related performance issues arise due to several factors, including blanking errors, dose errors, leveling and focusing offsets, proximity effects caused by backscattering, stitching errors, charging effects, electron beam drift over time, system contaminations (fogging, outgassing) and sample contaminations (particles) [12–14]. Charging effects can be mitigated by depositing a chromium layer on top of the photoresist

☆ This work is part of the Hamburg Quantum Computing (HQC) project, where the required technologies for the implementation of a quantum computer are developed. The project is co-financed by ERDF and Hamburg Ministry of Science, Research, Equalities and Districts (BWFGB).
* Corresponding authors.
E-mail addresses: matthias.vermeer@tuhh.de (M.L. Vermeer), nadeem.alhareeb@tuhh.de (N.K. Alhareeb), bojan.bosnjak@uni-hamburg.de (B. Bosnjak), lipka@tuhh.de (T. Lipka).
URL: https://www.tuhh.de/mst/startseite (M.L. Vermeer).

https://doi.org/10.1016/j.mne.2026.100359
Received 19 December 2025; Received in revised form 13 March 2026; Accepted 28 March 2026
Available online 30 March 2026
2590-0072/© 2026 The Authors. Published by Elsevier B.V. This is an open access article under the CC BY license (http://creativecommons.org/licenses/by/4.0/).

before exposure, while effects of focusing, proximity, and stitching can be addressed during the design phase.

Proximity effect correction (PEC) has been a topic of extensive research since the 1970s, with numerous design-based and dose-based correction schemes developed to compensate for electron scattering and improve pattern fidelity [15–18]. Initial approaches involved trial-and-error adjustments, but modern PEC employs computational models to predict and correct dose distributions systematically.

In this work, we investigate the influence of a design-based and a dose-based proximity correction approach for integrated photonic systems and address the effects of focusing and stitching. A microring resonator device in the all-pass configuration is used as test design and uniform and apodized grating coupler configurations are utilized for fiber-to-chip and chip-to-fiber coupling. Design variations are modeled and the designs are fabricated on an amorphous silicon on insulator (aSOI) platform. The systems are characterized and compared to theoretical computations to determine the influence of the proximity correction schemes.

Section 2 presents the employed methods, subdivided in the following parts: fabrication, layout, photonic system design, proximity effect, design-based proximity correction, dose-based proximity correction, comparison of proximity correction methods, optical characterization and analysis procedure. The results and discussion are reported in Section 3. Section 4 comprises the conclusions.

2. Methods

2.1. Fabrication

An amorphous silicon layer was deposited on top of a 4 inch wafer, which was used for the fabrication of exemplary integrated photonic test systems. The amorphous silicon layer was deposited using PECVD [19] and patterned using electron beam lithography. The integrated photonic structures were transferred into the amorphous silicon core layer using ICP-RIE (Oxford Cobra 100) and protected from dust by a TEOS-based silicon dioxide layer deposited using PECVD [20].

The CSAR AR-P 6200.13 positive tone resist was spun on the wafer (60 s/4000 rpm) and soft baked (60 s/150 °Celsius) to reach a thickness of 400 nm. After exposure, the sample was developed (AR 600-546, 60 s) and the development was abruptly stopped (AR 600-60, 30 s) followed by a DI water rinse.

The Raith Voyager machine was used for electron beam lithography (EBL), equipped with a 50 keV thermal field emission source, automatic focusing, write field calibration, and astigmatism correction. The wafer was loaded on the sample holder and fixed with three spring-clamp-based screws to hold the sample in place using minimal pressure, minimizing substrate bending. The sample was placed in the machine, evacuated, and initial focusing and astigmatism correction were performed. The beam column creates a focus depth of about 5 µm and uses a 2 nA beam current for the 60 µm aperture to reach a critical dimension of 12 nm. The maximum write field of $500 \cdot 500\,\mu\text{m}^2$ is used and an automatic stitching correction scheme is employed to reduce the stitching error to less than 15 nm. The sample was leveled by focusing at three edges of the sample and using piezo-motors to correct the sample height in order to have an identical local focus height. The position list containing all to-be-exposed design files was loaded and an automatic laser focusing routine was employed during writing. The machine refocused at those locations specified in the position list such that all following design files were exposed using a focus height within an area where the focusing offset was less than 5 µm. Edge markers were used for larger design files to fix the write field boundaries independent of the included systems. System designs were placed in the design file such that only wider waveguides crossed the write field boundaries to minimize propagation losses and functionality problems.

2.2. Layout

A microring resonator (MRR) in the all-pass (AP) configuration is used as test device in this work. Several other design files were included in the position list for other tests. Fig. 1 shows the layout for four subchips as well as zoom-ins of the design file layout for the AP MRR systems considered in this work. The layout is a negative of the designs (i.e. the blue areas are exposed) due to our use of a positive EBL resist and is created using a code-based design approach where the actual design (Object A) and a pattern surrounding the design with an additional 2 µm width to all sides (Object B) are XOR-ed in a step by-step approach to retain control over the design compartmentalization. The negative of the designs (i.e. the blue areas are exposed due to our use of a positive EBL resist) is created using a code-based design approach where the actual design (Object A) and a pattern surrounding the design with an additional 2 µm width to all sides (Object B) are XOR-ed in a step-by-step approach to retain control over the design compartmentalization.

In addition to the AP MRR test systems included in subchips 1 and 2, partial systems for exposure tests (subchip 3) and simple transmission systems for GC tests (subchip 4), including or excluding MRRs, were also utilized.

2.3. Photonic system design

The functionality of spectral components such as microresonators is based on the guided optical mode interfering with itself after a round trip of propagation through the resonator. The phase difference follows from the velocity of the optical wave, which can be described by the effective index of the waveguide n_{eff}, while the coupling between the bus and self-enclosed waveguide described by the coupled field coefficient k determines the quality of filtering at resonance. The AP MRR is schematically shown in Fig. 2(a) with the effective index (waveguide) and coupled field coefficient (directional coupler) computation regimes indicated. Computations of spectral characteristics of the MRR were performed using a simulation-based semi-analytical modeling framework (to be published elsewhere).

The fiber-chip coupling of light is performed using grating couplers (GCs), as shown in Fig. 2(b). The GC redirects the wave and reshapes the mode profile to overlap with that of a slab waveguide around a center wavelength λ specified by the Bragg condition:

$$n_{\text{grating}} = n_{\text{clad}} \cdot \sin(\theta) + m\frac{\lambda}{\Lambda}, \tag{1}$$

where n_{clad} is the cladding refractive index, Λ is the grating period, m is the order of diffraction and n_{grating} is the effective index of the grating structure. For a fully etched structure this is given by:

$$n_{\text{grating}} = F \cdot n_{\text{eff,g}} + (1 - F) \cdot n_{\text{eff,b}}, \tag{2}$$

with $F = l_b/\Lambda$ the fill-factor or duty cycle (and $\Lambda = l_b + l_g$) for the grating bar and etched gap lengths l_b and l_g, respectively, and with $n_{\text{eff,b}}$ and $n_{\text{eff,g}}$ the corresponding effective indices. A uniform GC uses a constant period and duty cycle, while for the apodized GC the period and duty cycle vary with location ($\Lambda(z)$ and $F(z)$).

GC computations were performed in COMSOL Multiphysics using a 2D model. Although neglecting the third dimensions results in over-exaggerated coupling efficiencies, the expected relation between the center wavelength and the period and duty cycle largely remains the same for an assumed slab with a width (in the out-of-plane x-direction) of 12 µm. The angle was set to $\theta = 8°$ and the fiber location, BOX thickness and cladding thickness were optimized prior to further parameter investigations. While for the uniform design the period and duty cycle were varied in simulations and in the design layouts, for apodized grating couplers a proven design was taken and only the duty cycle was varied by adding a constant proximity value p to each bar length and subtracting it from each gap length [21].

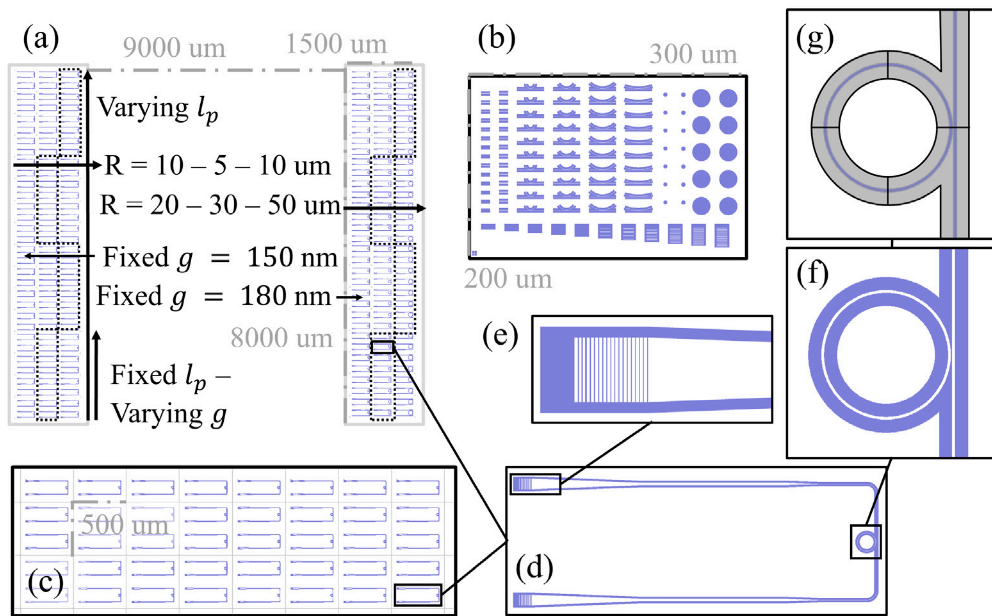

Fig. 1. Photonics EBL layout of (a) subchip 1 (left) and 2 (right) including some parameter variations, (b) subchip 3 containing exposure dose test systems and (c) subchip 4 containing either uniform grating coupler (UGC) design variations or apodized grating coupler (AGC) proximity variations. (d) Zoom-in of the AP MRR system. The negative of the photonic system core, i.e. the 2 μm wide grooves, is exposed (blue). The system is subdivided in zoom-ins of the (e) grating coupler and (f) microring and directional coupler segment. The four bend waveguide design blocks for a 10 μm ring are indicated in (g), where Object A (blue) and Object B (gray) are shown.

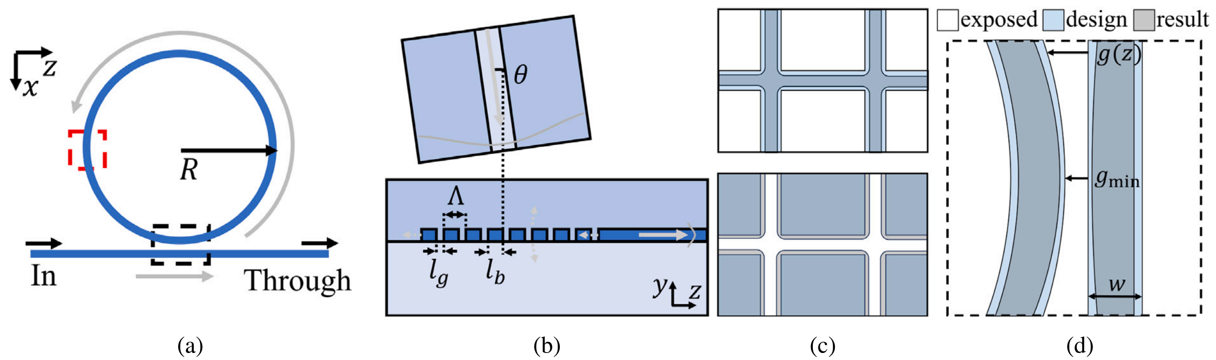

Fig. 2. Schematic of (a) a microring resonator (MRR) in the all-pass configuration, with the *In* and *Through* ports indicated, as well as the resonator radius R, the resonator waveguide (red box), the directional coupler (black box) and the direction of light propagation (gray arrow), (b) a grating coupler (GC) with the period Λ, bar length l_b and gap length l_g indicated, (c) intershape proximity (top) and intrashape proximity (bottom) and (d) shape deformation due to proximity for the directional coupler section of an MRR (black box in (a) rotated by 90°).

2.4. Proximity effect

The required exposure dose varies across the wafer in case of leveling and focusing issues, but was found to be relatively stable for the utilized automatic focusing and design file grouping. In case a single focusing point is chosen for lithography of the entire wafer, defocusing > 5 μm (i.e. more than the voxel size) results in an increase in the stitching error, a larger achievable minimum feature size and an increase in the required dose hence the writing time. Furthermore, the required exposure dose depends on the feature size and the feature spacing. The combined effect of forward scattering, the secondary electron traveling range and back-scattering results in resist exposure outside of the desired exposure area, which is called the *proximity effect*. For EBL this means that the exposure of a pixel also slightly exposes neighboring pixels.

The proximity effect can be observed in the pattern in two ways, intrashape and intershape proximity, as shown in Fig. 2(c). Intrashape proximity causes smaller design shapes to be underexposed compared to larger shapes, due to the smaller amount of exposed neighboring pixels. For positive resists this results in a narrowing of such small design shapes. Intershape proximity results in the accidental exposure of small spaces in-between larger design shapes, since the exposed areas cooperatively expose these not-to-be-exposed gaps. This results in the narrowing of smaller unexposed areas in densely packed design regions for positive-tone resists.

Intrashape proximity effects are generally applicable to all photonic systems created using positive resists. The exposed areas are relatively small to minimize overexposure of smaller feature sizes and reduce the writing time. For this reason, the dose-to-clear of larger circles is not directly applicable to the smaller photonic pattern and feature sizes and the practical exposure dose has to be determined for the design shapes under consideration. Intershape proximity is important for the grating coupler and directional coupler region. For the GC a larger area of roughly $4 \cdot 16\,\mu m^2$ is exposed to terminate the light path. This area results in overexposure of the grating coupler area and thus widening of the gaps and slimming of the bars. In the directional coupler region,

the small gap is overexposed by the neighboring patterns at both sides of the waveguide (east and west, see Figs. 1(f) and 2(c)) and by the comparatively large pattern area where the ring and bus waveguide come near to each other (north and south). Deviations in the severity of the proximity effects cause a deformation of the intended design shape (see Fig. 2(c)).

2.5. Design-based proximity correction

In the design-based proximity correction approach the size of each critical design element is adjusted by a corresponding proximity constant so as to obtain a result close to the intended design value. For example, as shown in Fig. 2(c), the resulting waveguide width w_r is expected to decrease as compared to the design width w_d while the resulting coupling gap $g_r(z)$ is enlarged compared to the design ($g_d(z)$). To compensate for this, we use $w_d = w_i + w_p$ and $g_{min,d} = g_{min,i} - g_p$ with subscripts r, d, i and p denoting the result, design layout, intended design and proximity values of the respective parameter. For the grating coupler we use $l_{b,d} = l_{b,i} + l_{b,p}$ and $l_{g,d} = l_{g,i} - l_{g,p}$ with $l_{b,p} = l_{g,p} = l_p$ the GC proximity. This procedure approximates the intended design dimensions but does not fully compensate for more complex shape distortions induced by proximity effects (see Fig. 2(c)).

The proximity values w_p, g_p, and l_p are determined experimentally by fabricating arrays with varied parameters and analyzing transmission measurements relative to theoretical expectations. Once established, this correction requires a single exposure dose for all adjusted designs, simplifying lithography.

2.6. Dose-based proximity correction

To correct for the proximity effect using variations of the exposure dose across the design, the energy density profile in the resist layer should be known. Several functions can be employed [22,23], where one of the most complete variants is the exponentially modified 3-term Gaussian form of the equation given by:

$$f(r) = \frac{1}{\pi(1+\eta_1+\eta_2+\nu)}\left(\frac{1}{\alpha^2}\exp\left[-\frac{r^2}{\alpha^2}\right] + \frac{\eta_1}{\beta_1^2}\exp\left[-\frac{r^2}{\beta_1^2}\right] + \frac{\eta_2}{\beta_2^2}\exp\left[-\frac{r^2}{\beta_2^2}\right] + \frac{\nu}{2\gamma^2}\exp\left[-\frac{r}{\gamma}\right]\right), \quad (3)$$

where parameters α, β_1, β_2, γ, η_1, η_2 and ν characterize forward scattering, back-scattering, and decay effects. Variations of the equation with 2 or 3 Gaussians (G) and 0 or 1 exponentials (e) were utilized.

The energy density distribution was obtained from Monte Carlo simulations in the Raith NanoPECS software suite, where one million electrons were launched into the material stack using a 50 keV beam with a 1 nm diameter. Their trajectory was computed for the incorporated SOI material stack (400 nm resist/200 nm Si/1 μm SiO_2/Si substrate). The material characteristics were pre-determined by the manufacturer [24]. The proximity function was extracted by fitting Eq. (3) to the lateral deposited energy density distribution in the middle of the resist layer. The results are shown in Fig. 3(a) and (b).

The design was partitioned into smaller design segments and the proximity function was utilized to correct the exposure dose of each individual design segment of the complete system layout with a segment-dependent correction factor f_D. The exposed energy at a segment i is computed for an by adding the dose contribution of all surrounding segments j up to a maximum lateral distance r_{ij} between the segments of 20 μm [7]:

$$E_i = V\sum_{j=1}^{N} f(r_{ij})D_j \quad (4)$$

The correction factor f_D for each segment i is the inverse of E_i normalized with respect to the computation dose D_0. In practice, $D = D_0 \cdot f_D$ with $f_D > 1$ where D is the exposure dose and D_0 is a design-file specific base dose. A more accurate dose map is obtained with more (smaller) dose-correction segments, but this significantly increases the dose-correction computation time. The partitioned design layouts of the resonator and GC, the dose-corrected design of the AP MRR system and the expected resist profile after exposure using the corrected dose map and development are shown in Fig. 3(c)–(f).

2.7. Comparison of proximity correction methods

Unlike the design-based correction approach, the dose-based correction method enables compensation for more complex design geometries — such as ring-bus or ring-ring coupling regions — without introducing deformations. However, this flexibility comes at the cost of requiring individual correction for each design, which can lead to significantly longer overall correction times depending on the extent of segment exposure overlap. For instance, in our implementation, dose-correction for subchip 4 took approximately 8 min, whereas designs with more overlapping features could require up to 10 h per write field.

An additional advantage of the dose-based approach is that correction and compartmentalization can be performed prior to exposure, thereby minimizing computational overhead during electron beam lithography (EBL). This pre-processing led to a reduction in exposure time from about 20 min to 10 min per design file when processing 96 systems. Conversely, design-based correction relies on uniform design offsets and a single exposure dose, resulting in negligible computational overhead.

In summary, while dose-based correction does not increase the actual write times for the systems we implemented, it becomes considerably more time-consuming than design-based correction for shapes of higher complexity.

2.8. Optical characterization

The optical characterization set-up contains an xy-alignment sample stage software-controlled by piezo-motors (PM) and a single fiber array unit (FAU) attached to a manually controllable z-axis arm. The FAU is fixed at an angle of 8° with respect to the surface to minimize GC back-reflections. A camera system (CCD) is mounted from above for vision and initial alignment of the FAU to the photonic systems. A Keithly tunable laser source (TLS) with manual 3-paddle polarization controller (PP) is connected to the input fiber of the FAU, while the output fiber is directly connected to the photodiode detector (PD). The FAU contains 16 outputs with a 127 μm spacing, which allows for the simultaneous alignment of input and output GC. A schematic of the measurement set-up is shown in Fig. 4(a).

In the semi-automatic measurement procedure employed for the optical characterization of integrated photonic components an xy-raster scan around the initial user-set location is performed. At the location with the maximum power, a wavelength sweep is performed and the measurement spectrum is stored. The system automatically moves to the next system according to a position list and the procedure is repeated.

2.9. Analysis procedure

The influence of the GC on the transmission spectrum of each system is first determined. The optical power (in dB) of the spectrum is fitted using a quadratic equation of the form $y = a_0 + a_2\left(x - x_0\right)^2$ within the 3 dB bandwidth around the maximum power, resulting in an analytical approximation of the GC envelope (the *GC fit*). The center wavelength and maximum power of the GC are extracted from the GC fit.

The actual GC envelope (i.e. the smoothed maximum) over the entire spectral bandwidth is also extracted (the *GC envelope*). The data is subtracted from the GC envelope to obtain a normalized and leveled transmission spectrum. The characteristics of each resonance within the spectrum are extracted as follows. First, the minimum transmission

Fig. 3. Monte Carlo simulations of (a) the electron trajectories and (b) the lateral energy distributions and the proximity function fits. Partitioned design layouts of (c) the resonator and directional coupler and (d) the GC. (e) The dose-corrected design of the AP MRR system and (f) the expected resist profile after exposure and development.

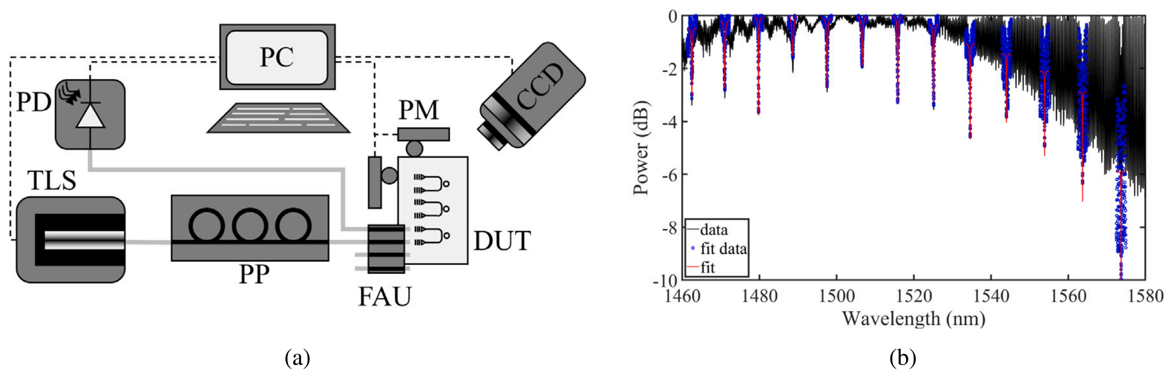

Fig. 4. (a) Schematic of the measurement set-up with light (solid gray) and control (dashed black) paths indicated. (b) Exemplary transmission data and fit of MRR resonances.

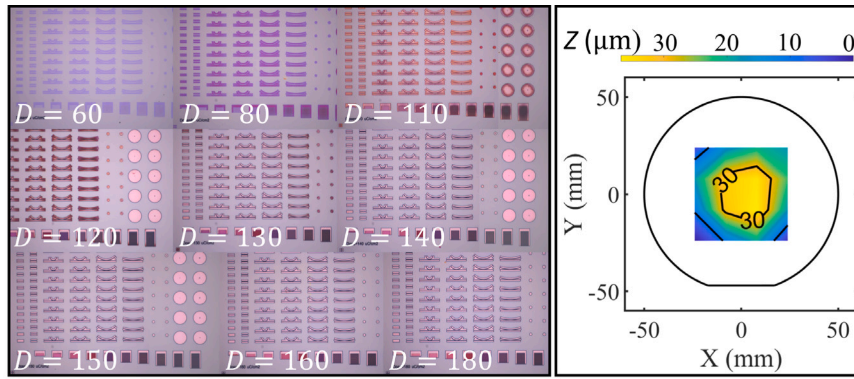

Fig. 5. (left) Test structures on aSOI exposed using several doses (μC cm^{-2}) and (right) the focus height variation across a standard SOI wafer normalized to the minimal measured value (at 16 locations on the wafer in a 16 by 16 mm raster).

value is determined within a bandwidth given by a user-defined FSR; the resonance is fitted on a linear scale (power in mW) within an FSR/6 bandwidth around this minimum value using a Lorentzian function:

$$y = a_0 + \frac{a_1}{(x - x_0)^2 + a_2}. \quad (5)$$

The Lorentzian fit parameters for the resonance are stored and the data one FSR higher is analyzed next. The procedure is repeated up to the maximum measured wavelength. The fit parameters are used to compute the resonance characteristics as follows: $\lambda_{\text{res}} = x_0$, FWHM = $2\sqrt{a_2}$, $Q = \lambda_{\text{res}}$/FWHM and FSR = $\lambda_{\text{res},m} - \lambda_{\text{res},m+1}$ with m the resonance peak number or mode order, while the ER is extracted from the unfitted normalized and leveled data since this parameter is strongly influenced by over- and under-fitting of the resonance peak. The FSR data for MRR groups is fitted using a linear function of the form $y = a_0 + a_2\,(x - x_0)$ with x_0 = 1550 nm to accurately determine the waveguide dispersion and radius-dependence.

Systems containing resonances with an average $ER < 3$ dB, a deviation of the GC center wavelength > 20 nm or transmitted power > 10 dB with respect to the average of the analyzed design group are filtered out and excluded from the analysis, since these systems suffer from dust particles, linewidth exposure deviations or etching inconsistencies. An exemplary Lorentzian fit to resonance data is shown in Fig. 4(b).

3. Results and discussion

3.1. Exposure dose

The influence of the proximity effect on the feature size of various design test shapes was investigated across a range of doses. An array of photonic test structures exposed at several selected doses is shown in Fig. 5 for the aSOI platform. Determining the dose-to-clear is more complex than initially expected, as it depends on the feature size. For an aSOI wafer a dose $D > 120$ μC cm^{-2} is required to fully develop larger structures with radii $r > 10$ µm. Features with radii $r = 0.5$ - 2 µm require a dose $D > 130$ μC cm^{-2} and a dose $D \approx 140$ μC cm^{-2} is required for features with radii $r = 0.1$ - 0.2 µm.

Furthermore, Fig. 5 also illustrates the focus height variations Z across a standard SOI wafer. These variations exceed the depth of focus, emphasizing the necessity to adjust the focus locally for each design file within a chip rather than applying a single focus setting for the entire wafer or each chip.

3.2. Design-based proximity correction

3.2.1. Uniform grating couplers

The transmission spectrum of uniform grating coupler systems with varying duty cycles and periods was measured and simulated. The envelope was extracted from the measured spectra for further analysis. The results were normalized with respect to the spectrum with the highest transmission and the center wavelength and relative maximum power were determined. Fig. 6 presents the center wavelength as a function of duty cycle and period for both measured and simulated data. The wavelength range within the maximum power window (transmission > −3 dB) is similar for the simulation and measurement data. Furthermore, the measured center wavelength exhibits a linear dependence on the duty cycle and period, consistent with theory (see Eqs. (1) and (2)). For a given period, the duty cycle and thus a proximity offset can be used to tune the center wavelength.

3.2.2. Apodized grating couplers

We measured spectra from 32 apodized microring resonator (AP MRR) devices. These devices were divided into 4 groups of 8 systems each, sharing the same AGC design proximity offset. Each group has a different proximity constant. Fig. 7(a) shows the measured spectra. Fig. 7(b) presents the relationship between center wavelength and proximity offset. This plot includes four measurement sets with 4 design groups each and two additional sets of 32 devices with a proximity constant l_p = 50 nm. A linear fit captures the trend well. This indicates that the proximity constant can tune the center wavelength while keeping transmitted power constant.

3.2.3. Microresonators

The coupling gap of microresonators (MRRs) was varied across four groups, each containing eight systems with a radius of R = 10 µm. The free spectral range (FSR) was well approximated by a linear fit (see Fig. 8). This indicates waveguide dispersion with wavelength. As expected, the FSR showed a negligible dependence on the coupling gap. Data at wavelengths less than 1480 nm and extinction ratio (ER) below 5 dB should be considered noise. These data correspond to GC design 1 in Fig. 7(a) and should be excluded from analysis. The remaining data show that smaller coupling gaps are optimal at shorter wavelengths. Larger gaps are required at longer wavelengths to maximize the extinction ratio. The theoretically required coupling gap to achieve critical coupling is approximately 160 nm. The practical optimal range of 140–150 nm suggest a desired proximity offset of 10–20 nm.

3.3. Dose-based proximity correction

3.3.1. Apodized grating couplers

To test the influence of a dose-based proximity correction scheme the AGC design was adjusted using 4 proximity functions (see Section 2.6) as compared to an unadjusted (default) design for several design specific doses D_0. The results are shown in Fig. 9. The white space in Fig. 9(a) indicates the split in two design files located 8 mm apart, which results in an offset due to processing differences. The offset was corrected for in Fig. 9(b).

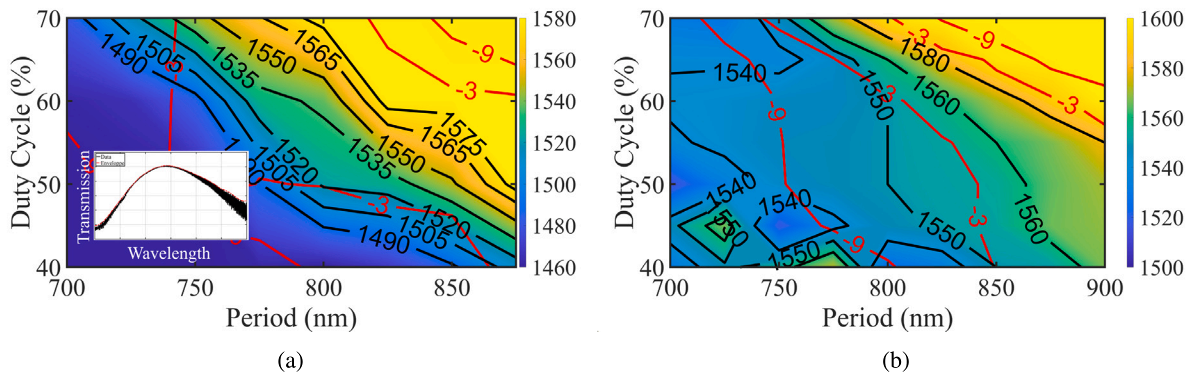

Fig. 6. Center wavelength of uniform grating coupler for the (a) measured systems and (b) simulated systems. The red lines indicate the relative transmission. The inset in (a) shows an exemplary measured spectrum and the envelope.

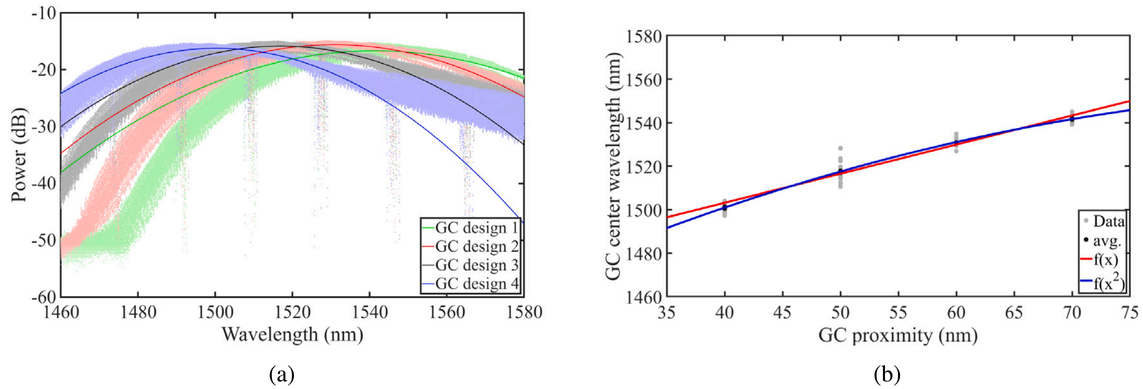

Fig. 7. (a) Transmission of apodized grating couplers for a different design proximity constant and a quadratic fit within the 3 dB bandwidth to the average of the spectra for each design group. The designs 1–4 correspond to a GC proximity of l_p = 70 - 40 nm. (b) Average center wavelength as a function of the proximity constant in the design and a fit to the data.

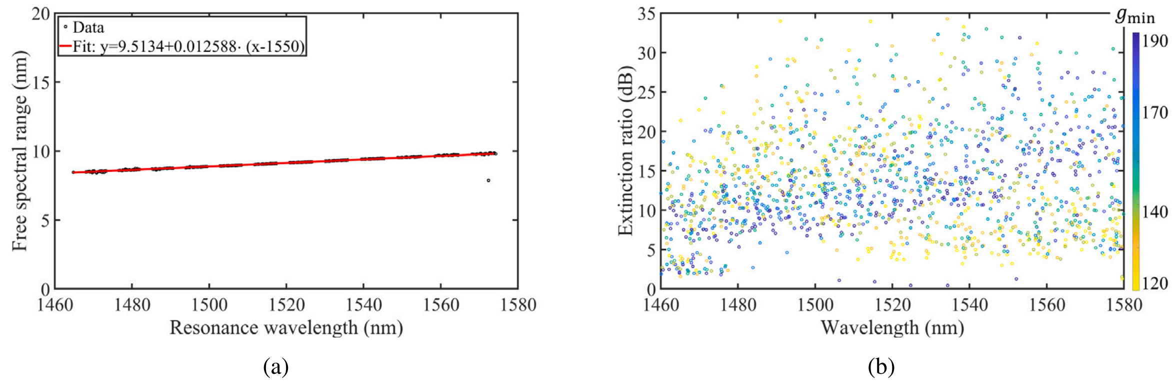

Fig. 8. (a) FSR and (b) ER for fitting all resonances in the transmission spectrum of 32 MRR devices with $R = 10\,\mu\text{m}$.

The main observable difference in the results is the dose offset for a given center wavelength. The transmission at the center wavelength was not significantly influenced by the proximity correction scheme. For an intended λ_{cen} = 1520 nm the design specific dose can be decreased from 120 down to 95 $\mu\text{C cm}^{-2}$ depending on the employed proximity function. The correction function f_D adjusts both the relative dose for the design segments with respect to each other and the absolute dose depending on the dimensions of the design shape (i.e. the minimum f_D and the range of f_D vary with the proximity function). The decrease in the required D_0 for obtaining the same center wavelength roughly corresponds to the average increase in f_D at the GC for each proximity function. For example, the default design is exposed with a constant $f_D = 1$ and D_0 = 120 $\mu\text{C cm}^{-2}$ resulting in D = 120 $\mu\text{C cm}^{-2}$, while the 3Ge design is exposed with f_D = 1.23 - 1.34 at the GCs and D_0 = 95 $\mu\text{C cm}^{-2}$ resulting in D = 116 - 127 $\mu\text{C cm}^{-2}$, such that the average D at the GC is the same. The shape adjustments resulting from the dose variations at the GC do not significantly influence the performance in terms of transmitted power or bandwidth. Dose correction of the GC does not improve over a design adjustment.

3.3.2. Microresonators

A set of $R = 50\,\mu\text{m}$ AP MRR systems containing different gap sizes was fabricated without proximity correction and with the 3Ge proximity correction scheme. The dose D_0 was scaled such that the AGC received the same average dose in both cases. The results are

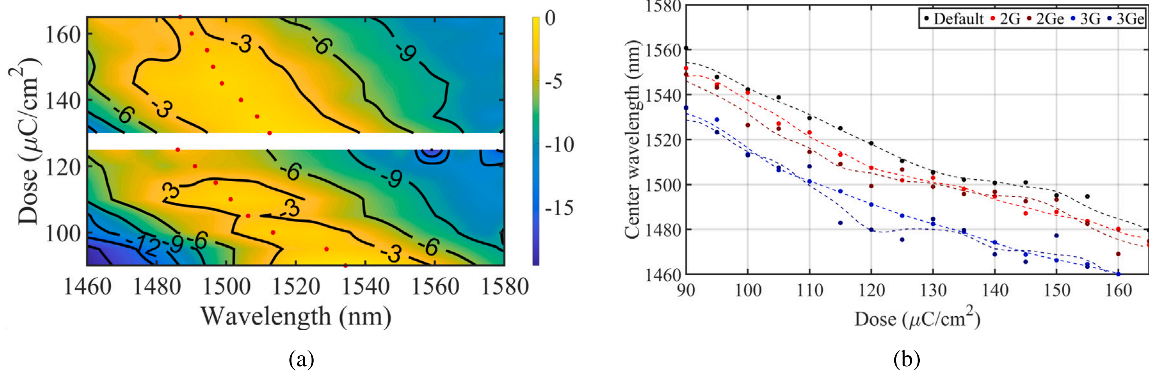

Fig. 9. (a) Transmission of apodized grating coupler design dose-corrected using the 3G function. The center wavelength is indicated (red circles) as a function of the design-specific dose D_0. (b) Center wavelength of apodized grating coupler designs dose-corrected using different proximity functions. Dashed lines show cubic splines to guide the eye.

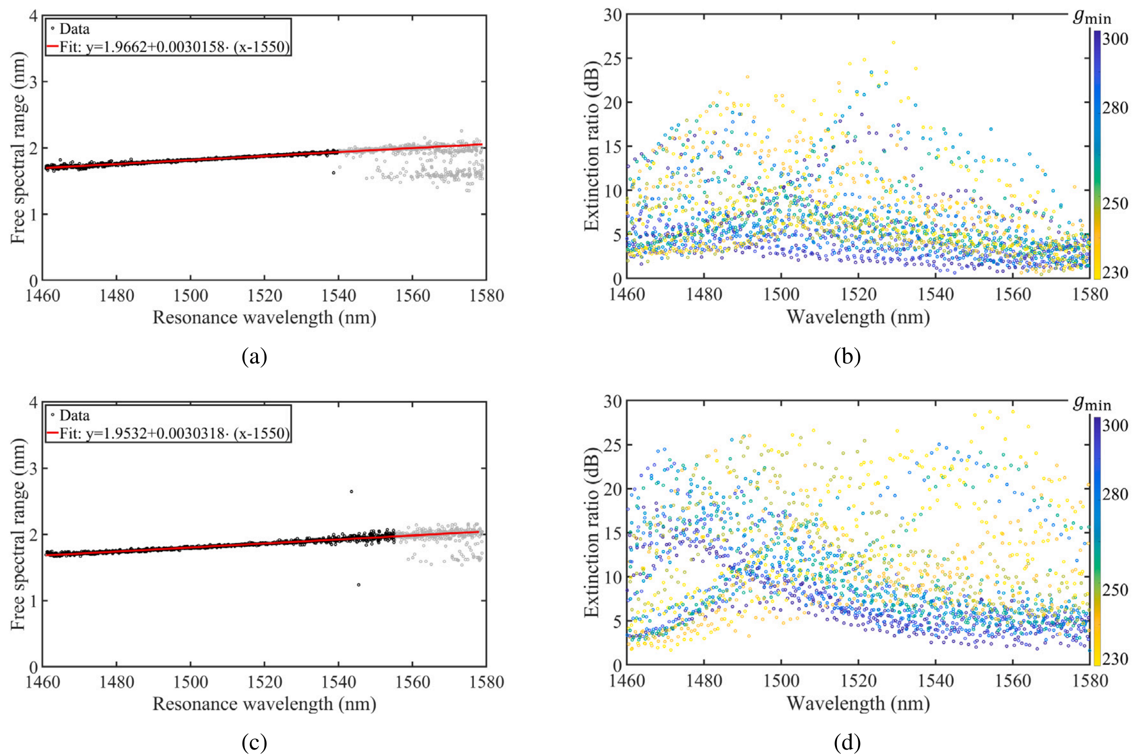

Fig. 10. Results for fitting all resonances in the transmission spectrum of 32 MRR devices with $R = 50\,\mu m$. (a) FSR and (b) ER for the default designs and (c) FSR and (d) ER for the 3Ge dose-corrected designs. The FSR data used for the fit (black) is shown separate to the unused set of data (gray).

shown in Fig. 10. For the 3Ge-corrected AP MRR designs, a clearer trend in the extinction ratio (ER) variation with wavelength as a function of coupling gap was observed compared to the uncorrected designs. Additionally, the optimal design showed a higher ER when dose correction was applied.

3.4. Comparison of proximity correction methods

A comparison of the methods shows that both design-based and dose-based proximity correction effectively compensate for proximity effects. Dose-based correction achieves somewhat higher accuracy in device performance metrics due to its ability to correct complex shapes precisely. A simultaneous dose correction of both the resonator and grating coupler leads to an improved overall system performance and a single system optimum. Design-based correction offers a practical trade-off, enabling rapid implementation with a single exposure dose and no additional computational effort while achieving reasonable accuracy.

4. Conclusions

We investigated the effects of both design-correction and dose-correction procedures on mitigating proximity effects. The design-correction approach applies fixed offsets to design parameters, such as the grating coupler (GC) duty cycle and the resonator coupling gap, resulting in a general system optimization. A duty cycle offset for uniform grating couplers (UGCs) or a proximity offset for apodized grating couplers (AGCs) leads to a linear adjustment of the center wavelength. For the fabricated systems in this work, a fixed coupling gap offset of 20 nm was required to achieve critical coupling compared to theoretical expectations.

Alternatively, proximity correction models using two or three Gaussian (G) functions with zero or one exponential (e) function to modify the dose distribution across the design were employed. The AGCs designed with different models operated at similar center wavelengths

and showed comparable coupled power for the same effective dose. Moreover, the 3Ge model yielded microresonator systems with overall higher extinction ratios.

In summary, design-based correction provides a simpler and faster approach suitable for rapid prototyping, while dose-based correction better compensates complex proximity effects at the expense of increased computational time. The choice of method should balance desired accuracy and available processing resources.

CRediT authorship contribution statement

Matthias L. Vermeer: Conceptualization, Fabrication, Methodology, Design, Lay-out, Data acquisition, Data analysis, Writing – original draft and final manuscript. **Nadeem K. Alhareeb:** Fabrication. **Bojan Bosnjak:** Fabrication, Writing - fabrication review. **Robert H. Blick:** Supervision, Writing - review. **Timo Lipka:** Design, Lay-out, Measurement set-up preparation, Resource acquisition, Supervision, Writing - review and editing. **Hoc Khiem Trieu:** Resource acquisition, Supervision, Writing - review.

Declaration of competing interest

The authors declare that they have no known competing financial interests or personal relationships that could have appeared to influence the work reported in this paper.

Data availability

Data will be made available on request.

References

[1] J. Sharma, Z. Xuan, H. Li, T. Kim, R. Kumar, M.N. Sakib, C.M. Hsu, C. Ma, H. Rong, G. Balamurugan, J. Jaussi, Silicon photonic microring-based 4 × 112 Gb/s WDM transmitter with photocurrent-based thermal control in 28-nm CMOS, IEEE J. Solid-State Circuits 57 (4) (2022) 1187–1198, http://dx.doi.org/10.1109/jssc.2021.3134221.

[2] A. Shen, C. Qiu, L.Z. Yang, T.G. Dai, Y.L. Hao, X.Q. Jiang, J.Y. Yang, Integrated reconfigurable microring based silicon WDM receiver for on-chip optical interconnect, J. Opt. 17 (5) (2015) 055801, http://dx.doi.org/10.1088/2040-8978/17/5/055801.

[3] C. Demirkiran, F. Eris, G. Wang, J. Elmhurst, N. Moore, N.C. Harris, A. Basumallik, V.J. Reddi, A. Joshi, D. Bunandar, An electro-photonic system for accelerating deep neural networks, ACM J. Emerg. Technol. Comput. Syst. 19 (4) (2023) http://dx.doi.org/10.1145/3606949.

[4] H. Zhang, M. Gu, X.D. Jiang, J. Thompson, H. Cai, S. Paesani, R. Santagati, A. Laing, Y. Zhang, M.H. Yung, Y.Z. Shi, F.K. Muhammad, G.Q. Lo, X.S. Luo, B. Dong, D.L. Kwong, L.C. Kwek, A.Q. Liu, An optical neural chip for implementing complex-valued neural network, Nat. Commun. 12 (1) (2021) http://dx.doi.org/10.1038/s41467-020-20719-7.

[5] J. Bao, Z. Fu, T. Pramanik, J. Mao, Y. Chi, Y. Cao, C. Zhai, Y. Mao, T. Dai, X. Chen, X. Jia, L. Zhao, Y. Zheng, B. Tang, Z. Li, J. Luo, W. Wang, Y. Yang, Y. Peng, D. Liu, D. Dai, Q. He, A.L. Muthali, L.K. Oxenløwe, C. Vigliar, S. Paesani, H. Hou, R. Santagati, J.W. Silverstone, A. Laing, M.G. Thompson, J.L. O'Brien, Y. Ding, Q. Gong, J. Wang, Very-large-scale integrated quantum graph photonics, Nat. Photonics 17 (7) (2023) 573–581, http://dx.doi.org/10.1038/s41566-023-01187-z.

[6] W. Luo, L. Cao, Y. Shi, L. Wan, H. Zhang, S. Li, G. Chen, Y. Li, S. Li, Y. Wang, S. Sun, M.F. Karim, H. Cai, L.C. Kwek, A.Q. Liu, Recent progress in quantum photonic chips for quantum communication and internet, Light.: Sci. Appl. 12 (1) (2023) http://dx.doi.org/10.1038/s41377-023-01173-8.

[7] N. Pala, M. Karabiyik, Electron beam lithography (EBL), in: B. Bhushan (Ed.), Encyclopedia of Nanotechnology, Springer Netherlands, 2016, pp. 1033–1057, http://dx.doi.org/10.1007/978-94-017-9780-1_344.

[8] A.A. Tseng, Recent developments in electron beam lithography, J. Vac. Sci. Technol. B 21 (6) (2003) 2622–2643, http://dx.doi.org/10.1116/1.1613653.

[9] K. Li, J. Li, C. Reardon, C.S. Schuster, Y. Wang, G.J. Triggs, N. Damnik, J. Müenchenberger, X. Wang, E.R. Martins, T.F. Krauss, High speed e-beam writing for large area photonic nanostructures — a choice of parameters, Sci. Rep. 6 (1) (2016) http://dx.doi.org/10.1038/srep32945.

[10] A. Mirza, F. Sunny, P. Walsh, K. Hassan, S. Pasricha, M. Nikdast, Silicon photonic microring resonators: a comprehensive design-space exploration and optimization under fabrication-process variations, IEEE Trans. Comput.-Aided Des. Integr. Circuits Syst. 41 (10) (2022) 3359–3372, http://dx.doi.org/10.1109/tcad.2021.3132555.

[11] T. Lipka, J. Muller, H.K. Trieu, Systematic nonuniformity analysis of amorphous silicon-on-insulator photonic microring resonators, J. Lightwave Technol. 34 (13) (2016) 3163–3170, http://dx.doi.org/10.1109/JLT.2016.2549738.

[12] D.C. Joy, Proximity effect correction in electron beam lithography: Monte Carlo simulation and experiments, J. Appl. Phys. 71 (6) (1992) 3225–3230, http://dx.doi.org/10.1063/1.351804.

[13] Y.C. Chen, Proximity effect correction for electron beam lithography by variable shaped beams, Microelectron. Eng. 53 (2000) 299–302, http://dx.doi.org/10.1016/S0167-9317(99)00564-2.

[14] K.H. Lee, I.S. Kim, S.J. Kwon, New proximity effect correction algorithm for electron beam lithography, J. Micromech. Microeng. 21 (2011) 095018, http://dx.doi.org/10.1088/0960-1317/21/9/095018.

[15] A.N. Parikh, Proximity effect correction in electron-beam lithography, IBM J. Res. Dev. 21 (1) (1977) 68–74, http://dx.doi.org/10.1147/rd.211.0068.

[16] B. Lee, T. Hashimoto, I. Grinberg, A novel dose modulation technique for proximity effect correction in electron beam lithography, J. Vac. Sci. Technol. B 9 (6) (1991) 3243–3247, http://dx.doi.org/10.1116/1.585669.

[17] M.A. Reed, Proximity effect correction using shape fracturing and dose modulation, J. Vac. Sci. Technol. B 11 (6) (1993) 2519–2523, http://dx.doi.org/10.1116/1.587741.

[18] D.B. Suyatin, A.V. Yakimov, R.A. Yakimova, Proximity effect correction for electron beam lithography of graphene, Appl. Phys. Lett. 89 (2006) 153121, http://dx.doi.org/10.1063/1.2358938.

[19] A. Harke, M. Krause, J. Mueller, Low-loss singlemode amorphous silicon waveguides, Electron. Lett. 41 (25) (2005) 1377–1379, http://dx.doi.org/10.1049/el:20052387.

[20] M.L. Vermeer, H.K. Trieu, T. Lipka, Characterization of TEOS-based SiO2 for integrated photonics, in: MikroSystemTechnik Kongress 2023, 2023, pp. 1–5.

[21] T. Lipka, L. Moldenhauer, J. Mueller, H.K. Trieu, Photonic integrated circuit components based on amorphous silicon-on-insulator technology, Photonics Res. 4 (3) (2016) 126–133, http://dx.doi.org/10.1364/PRJ.4.000126.

[22] J. Shapiro, M. Kahl, L.V. Litvin, Measurement of short-range PSF in EBL, Micro Nano Eng. 22 (2024) 100238, http://dx.doi.org/10.1016/j.mne.2024.100238.

[23] S. Aya, K. Kise, H.Y. Hideki Yabe, K.M. Kenji Marumoto, Validity of double and triple gaussian functions for proximity effect correction in X-ray mask writing, Japan. J. Appl. Phys. 35 (3R) (1996) 1929–1936, http://dx.doi.org/10.1143/jjap.35.1929.

[24] L. Stevens, R. Jonckheere, E. Froyen, S. Decoutere, D. Lanneer, Determination of the proximity parameters in electron beam lithography using doughnut-structures, Microelectron. Eng. 5 (1–4) (1986) 141–150, http://dx.doi.org/10.1016/0167-9317(86)90040-7.